A lateral-torsional buckling demonstration model using 3D printing

L. N. Virgin[a], P. S. Harvey Jr.[b,*]

[a]*Department of Mechanical Engineering and Materials Science, Duke University, Durham, NC, USA*
[b]*School of Civil Engineering and Environmental Science, University of Oklahoma, Norman, OK, USA*

Abstract

It is well-established that beams of relatively narrow cross-section have a tendency to buckle laterally when loaded. This type of lateral-torsional instability, which has considerable practical importance in a variety of thin-walled structures, is a classical buckling situation in which the critical load is related, among other things, to characteristic features of the cross-section. In this short paper, 3D-printing is exploited to provide a parametric study based on a fixed cantilever geometry in which a number of standard cross-sectional forms are compared in terms of their effect on this kind of buckling behavior.

Keywords: lateral, torsion, buckling, 3D-printing, engineering education

1. Introduction

In fundamental beam theory, bending deflection is inversely proportional to flexural rigidity, EI, where the Young's modulus E is the familiar elastic material property and I is the second moment of area. This second moment of area relates to the geometric distribution of the material about the neutral axis, and provides the motivation for using an I-section in resisting uni-directional bending for example. However, if the load is applied away from the centroid, or if a section does not possess an axis of symmetry, then the deflection is typically accompanied by some twisting, and the role of the shear center becomes paramount. In addition, if the cross-section is sufficiently slender (in the direction of loading) and the section has relatively low lateral and torsional stiffness, the advent of lateral-torsional buckling (LTB) may occur [1–8]. The torsional rigidity GJ plays an

*Corresponding author.
Email address: harvey@ou.edu (P. S. Harvey Jr.)

important role, where G is the shear modulus for the material, and J is the polar second moment of area, or torsional constant. The motivation for this paper is largely educational [9–12]. Some measurements are made, and they help to highlight the sensitive nature of buckling relative to theoretical estimates of critical loads based on theory together with verification using the finite element capabilities of Fusion 360.

2. Background

A beam may buckle with a combination of out of plane and twisting behavior if loaded in its nominally stiffer direction. Resistance to this type of behavior depends on the bending and torsional stiffness of the cross section. In this paper we consider a specific beam configuration, a cantilever, with length L. Under the action of an end-load it can be shown that the critical buckling load, $F_{cr}P_{cr}$, is given by [13–16]

$$F_{cr} = \frac{4.013}{L^2}\sqrt{EI_yGJ} \tag{1}$$

assuming the end load F is applied at the centroid of the section. Applying the load a distance y_p above the centroid changes this equation to

$$F_{cr} = \frac{4.013}{L^2}\sqrt{EI_yGJ}\left[1 - \frac{y_p}{L}\sqrt{\frac{EI_y}{GJ}}\right]. \tag{2}$$

Note that Eqs. (1) and (2) assume that $L^2GJ/EC_w \to \infty$, which is the case if the warping constant $C_w = 0$ (i.e., rectangular cross section) or beam is very long (i.e., L very large). We seek to investigate Eqs. (1) and (2) in the following systematic way: changing the cross-sectional shape and hence I and J, and the load location y_p. In addition, a horizontal offset of the load application point is also studied in terms of breaking the symmetry of the system. Throughout, the boundary conditions, length, and material properties all are fixed.

3. The baseline geometry

A standard 'baseline' geometry is selected in order to later compare the LTB behavior of beams with different cross sections. Fig. 1 shows the baseline geometry, for which the following dimensions are selected: The length L of the beam is 200 mm, and the cross section is rectangular

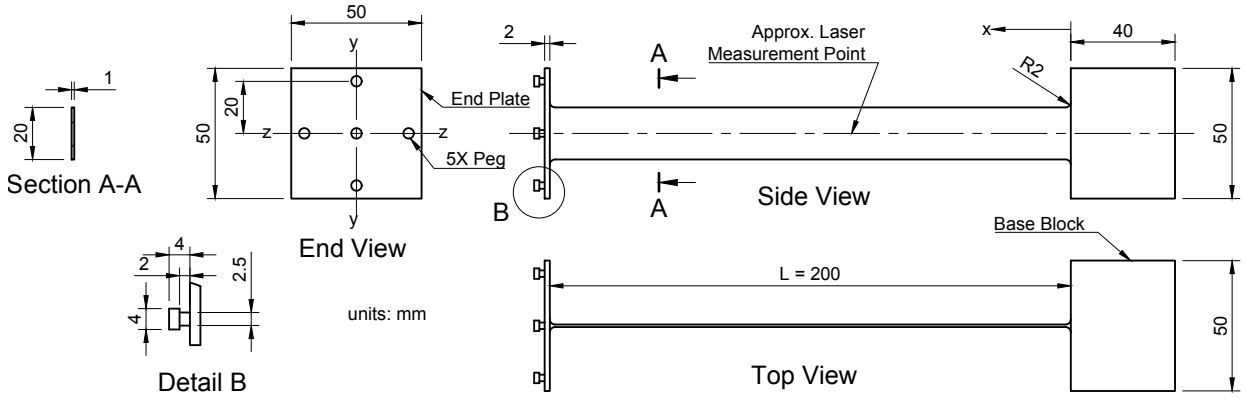

Figure 1: Drawing of baseline geometry with rectangular cross section. Nominal dimensions shown.

with width $b = 1$ mm and depth $d = 20$ mm. The beam is cantilevered from a base block, which provides fixed boundary conditions. At the free end of the beam, a 50 mm × 50 mm end plate provides five loading points (pegs) located at the cross section's centroid, ±20 mm from the weak axis (y-y), and ±20 mm from the strong axis (x-x). Small (2-mm) fillets are included at the beam/block and beam/end plate interfaces to minimize stress concentrations.

The Young's modulus E and Poisson's ratio μ for the ABS thermoplastic used in this study were taken to be 2.1 GPa and 0.38, respectively [17]. The shear modulus $G = E/[2(1+\mu)] = 0.76$ GPa. With these material properties, the flexural rigidity $EI_y = Eb^3d/12 = 3500$ N·mm^2 and the torsional rigidity $GJ = Gb^3d/3 = 5100$ N·mm^2 for the baseline (rectangular) geometry. With these specific values, the LTB load at the centroid (Eq. (1)) is $F_{cr} = 0.423$ N, corresponding to a hanging mass of 43.1 g. If the load application is moved to a point 20 mm below the centroid ($y_p = -20$ mm in Eq. (2)), then $F_{cr} \rightarrow 0.388$ N (39.5 g); when moved 20 mm above the centroid ($y_p = +20$ mm), $F_{cr} \rightarrow 0.458$ N (46.7 g).

3D modeling of the part was performed in Fusion 360 (Autodesk, v2.0.12392). In addition to generating the STL file needed for 3D printing, Fusion 360 also has simulation tools, including structural buckling studies using finite element analysis (FEA) [18, 19]. For students, in addition to introducing them to advanced analysis tools, this feature is convenient to check their design prior to printing to ensure the design is reasonable for the testing setup and any limitations. Fig. 2(a) shows the FEA model of the baseline geometry. A new material was defined based on the specific

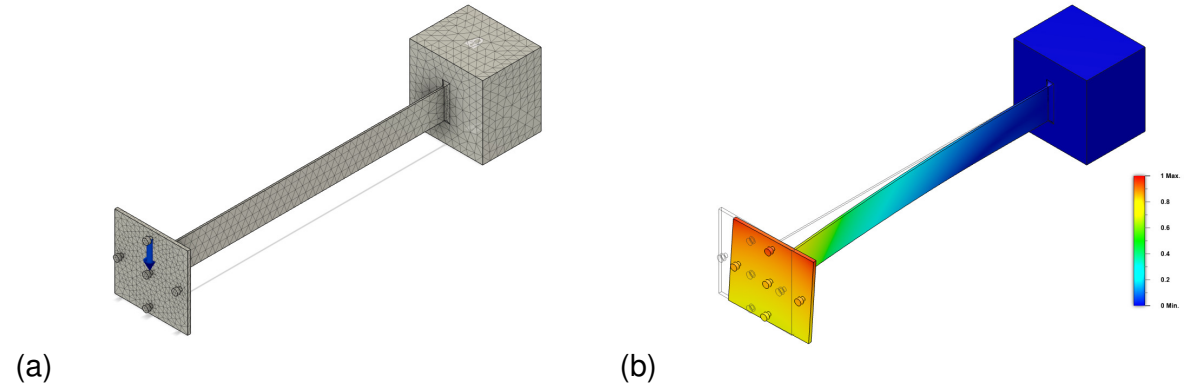

Figure 2: Fusion 360 results for the baseline geometry with rectangular cross section and load applied at the middle peg: (a) finite element model and (b) first buckling mode.

ABS thermoplastic properties used. Structural constraints were used to fix the top and bottom of the base block, and a 1-N downward load was applied to the peg. For the buckling study, default settings were used with the exception of the model-based, average element size which was reduced to 3% for greater accuracy. The results of the analysis for a load applied to the middle peg on the baseline geometry is shown in Fig. 2(b). The corresponding buckling load is given in Table 1. Note that in Table 1 two buckling loads are reported—a positive load in the direction of the applied load (i.e., downward), and a negative load in the opposite direction (i.e., upward). For the case of the middle-peg load, these two values are equal in magnitude, as expected. The (downward) LTB load is smaller when applied at the top and larger when applied at the bottom, confirming Eq. (2). The (downward) LTB load is smaller when applied at the left and right than when applied at the middle (even though this is no longer strictly a buckling problem), with some slight asymmetry due to modeling tolerances.

4. Cross section variations

We then depart from the baseline case in order to assess the effect of modifying the cross section. The 1 mm $\times$ 20 mm rectangle from the baseline case is retained as the web of T-shape, I-shape, Z-shape, and C-channel sections. These shapes are formed by including 1-mm-thick, 4-mm-wide flanges (or legs) to the top and bottom of the web. Small (1-mm) fillets are used between the web and flanges for the I-shape, Z-shape, and C-channel, but not the T-shape. Fig. 3 shows the

Table 1: LTB loads [N] calculated using Fusion 360 for different load application locations. The two values given correspond to loads applied downward (↓) / upward (↑).

Cross section	Load application location				
	Top	Left	Middle	Right	Bottom
Rectangle	0.396 / 0.479	0.430 / 0.438	0.441 / 0.441	0.434 / 0.431	0.479 / 0.396
T-shape	0.815 / 1.33	0.921 / 1.19	0.957 / 1.15	0.985 / 1.02	1.07 / 0.874
I-shape	1.47 / 2.17	1.86 / 1.87	1.87 / 1.87	1.87 / 1.86	2.17 / 1.47
Z-shape	1.70 / 2.92	2.46 / 2.34	2.41 / 2.41	2.34 / 2.46	2.92 / 1.70
C-channel	1.77 / 3.23	2.74 / 2.75	2.64 / 2.64	2.50 / 2.50	3.23 / 1.78

nominal dimensions of the sections along with their location on the end plate (i.e., centered on the rectangular web). The I-beam (Fig. 3(b)) is doubly symmetric, so the middle peg is located at the center of the end plate. While having no axes of symmetry, the Z-shape (Fig. 3(c)) also has the middle peg located at the center of the end plate, which is coincident with the section's centroid and shear center. For the other two sections, which have single symmetry or "monosymmetry", the middle peg is shifted. For the T-shape (Fig. 3(a)), the middle peg is located at the section centroid, 1.75 mm above the center of the end plate. For the C-channel (Fig. 3(c)), the middle peg is located approximately at the shear center, 1 mm left of center. In all cases, left and right pegs are located at the same location with respect to the center of the end plate. The top and bottom pegs are in the same locations with respect to the center of the end plate, except for the C-channel (Fig. 3(d)) which has the top and bottom pegs aligned with the middle peg.

Given the cross-sectional dimensions we expect the critical loads to scale according to the entries in Table 2, for central loading. The predicted LTB loads for the T-shape, I-shape, Z-shape, and C-channel sections calculated with Fusion 360 are given in Table 1.

5. 3D printing of slender structures

Five cantilevers with different cross-sections were printed on a Stratasys 3D-printer using ABS thermoplastic, according to the parameters described. A photographic image of the basic experi-

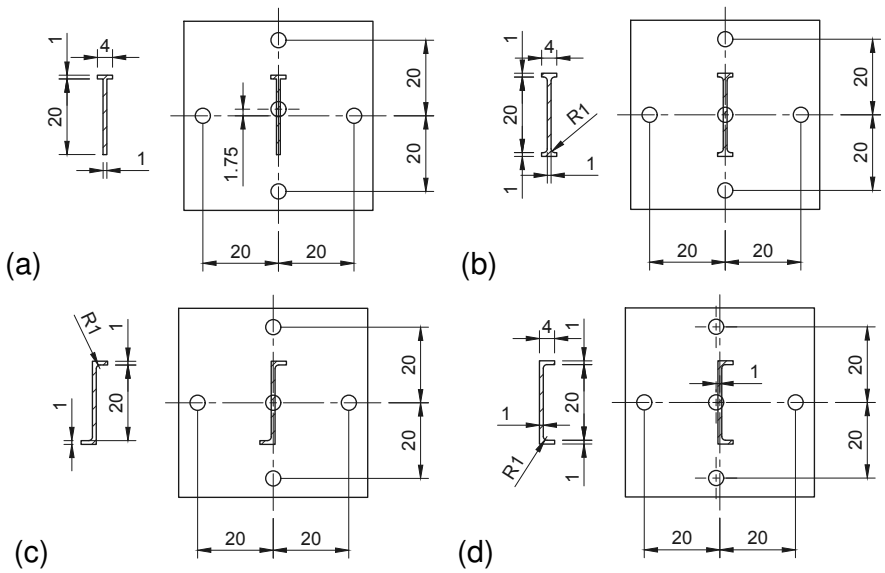

Figure 3: Variations in the cross sections: (a) T-shape, (b) I-shape, (c) Z-shape, and (d) C-channel. Units: mm.

mental set-up is shown in Figure 4, with the unloaded cantilever shown in part (a) including the laser proximity sensor, and the loaded (buckled) system in part (b).

Owing to inevitable resolution limitations of the printer, the actual parameters of the printed parts differ slightly from the nominal design values. Specifically, the 'wall' thickness tended to have a slightly greater dimension than designed. It is also worth pointing out that in comparing

Table 2: Cross-sectional properties for the various shapes with nominal dimensions: web = (20 mm × 1 mm), flange = (4 mm × 1 mm). *based on the formula $Uh^3/3$, where U is the middle line.

Cross section	J^* [mm^4]	I_y [mm^4]	$\sqrt{I_y J}$ [mm^4]	$\frac{\sqrt{I_y J}}{\sqrt{(I_y J)_{\text{rect}}}}$ [–]
Rectangle	6.67	1.67	3.34	1.0
T-shape	8.17	7.00	7.56	2.26
I-shape	9.67	12.33	10.92	3.27
Z-shape	9.33	30.3	16.81	5.03
C-channel	9.33	48.5	21.27	6.37

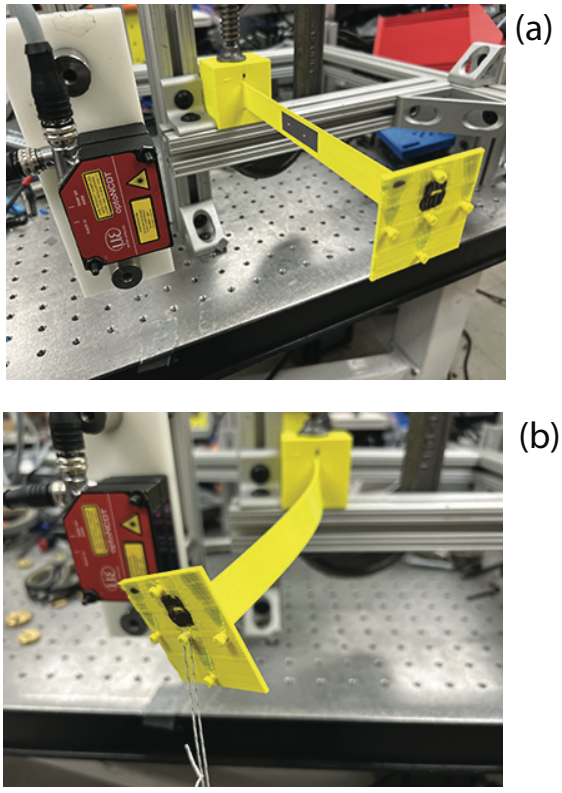

Figure 4: Experimental arrangement, rectangular cross-section: (a) unloaded system, and (b) post-buckled system.

with theory, we assume the elastic moduli values based on standard specifications. The Young's modulus and shear modulus are not quite exact values, with a slight dependence on print orientation, small amounts of anisotropy, and imperfections in general [17].

Weights were added to each of the various pegs sequentially and corresponding lateral deflection measured at a point near mid-span of the cantilever $(0.3 < x/L < 0.6)$. All the subsequent plots are simply vertical force (weight) versus lateral deflection δ. The phenomenon of buckling corresponds to the increase in the rate of change of deflection with load, rather than a specific load.

6. Experimental testing results

In this section, we present the results of placing weights of increasing magnitudes at the free ends of slender cantilevers liable to buckle in a lateral-torsional sense.

We start with the simple rectangular cross-section. In Figure 5, the results of placing the weights at the five peg locations are shown. When loaded at the centroid of the cross-section the

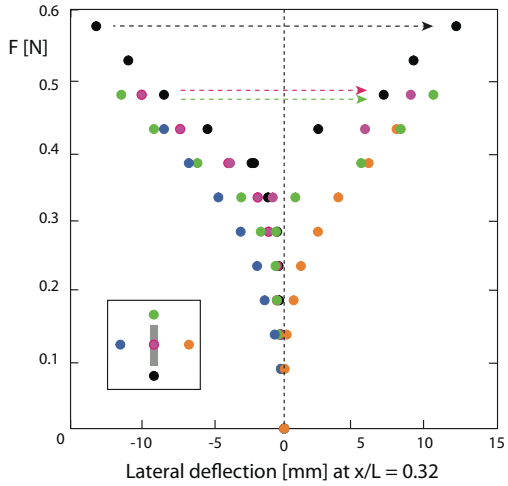

Figure 5: Experimental results for the narrow rectangular cross-section.

beam buckles in a clear preferred (left) direction, and this is true for any loading on the central vertical axis. It is only when loaded at the right peg that the beam buckles in the other (right) direction. Here, when the beam is heavily in its post-buckled state, it is moved across to its complementary post-buckled configuration (indicated by the dashed lines). Despite the relatively high resolution of the printer, the specific estimate of the critical buckling load (0.441 N) only provides a rough guide to the buckling instability. Although not conclusive, the critical load associated with the upper peg is slightly higher than the critical load associated with loading via the lower peg.

The results for the T-shaped cross-section (see Figure 3(a)) are shown in Figure 6. The 'upright' T-shape has a critical load of 0.957 N, and the 'downward' critical load of 1.15 N. In both orientations (simply rotating the cross-section through 180 degrees), the buckling deformation proceeds in the leftward direction (looking onto the end of the cantilever).

The I-shape results are shown in Figure 7, with an increase in the buckling load as expected. The Z-shape results are shown in Figure 8. Given the anti-symmetric nature of this cross section, it is not surprising that this system has a strong directional preference, even for low levels of loading. Finally, the C-channel results are shown in Figure 9. In this case the central peg was located at the shear center of the cross-section. This is the section most resistant to lateral-torsional buckling.

We can summarize these results by superimposing them as shown in Figure 10. In each of the data sets, the 'natural' load path is shown for each cross-section, and each beam is loaded at its

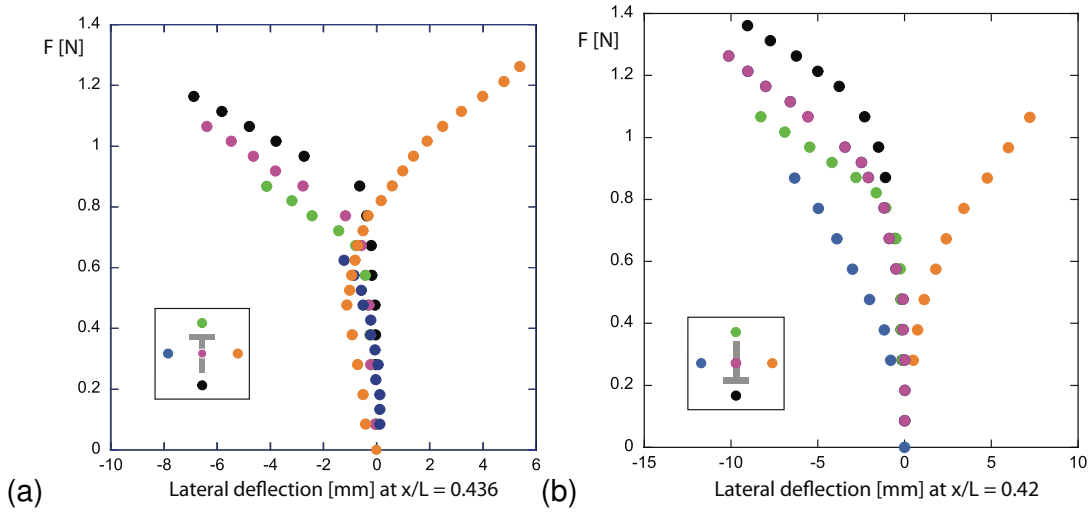

Figure 6: Experimental results for (a) the narrow T-shape cross-section and (b) the narrow 'upside down' T-shape cross-section.

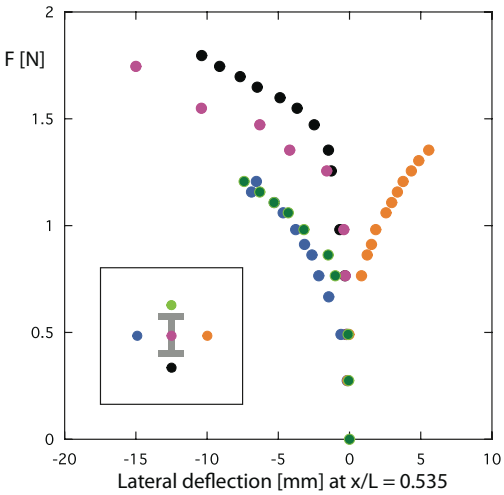

Figure 7: Experimental results for the narrow I-shape cross-section.

centroid/shear center (i.e., middle peg). The horizontal dashed lines correspond to the theoretical values obtained from Fusion 360 (and color-coded accordingly).

7. Southwell Plot

Despite the fact that the theoretical estimate for the critical LTB load is a specific number, an eigenvalue, it is clear from the experimental results that initial geometric imperfections and symmetry-breaking effects in general play an important role, and make practical estimates of the

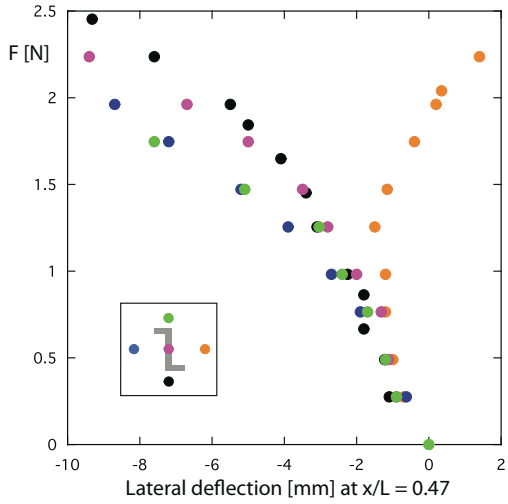

Figure 8: Experimental results for the narrow Z-shape cross-section.

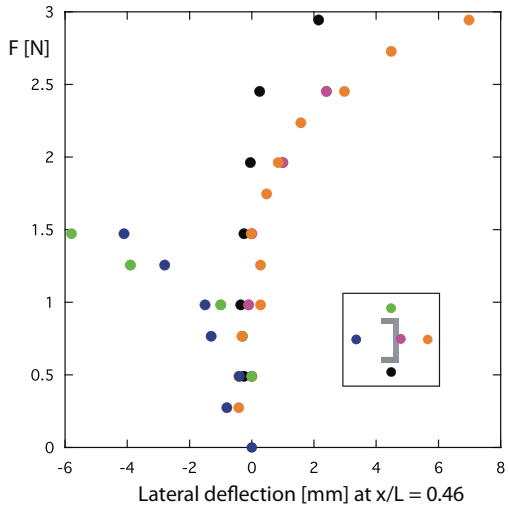

Figure 9: Experimental results for the narrow C-channel cross-section.

buckling load challenging. It is clear that in the vicinity of buckling there is an increases in the rate of deflection, sometimes referred to as a 'knee' in the data. In Figure 10(a), this relatively sudden increase in deflection does indeed occur where the 'perfect' system would buckle.

This rate of increase in deflection was recognized by Southwell [20], who realized that plotting deflection/load versus deflection would result in a straight line, with the important consequence that the (reciprocal of the) slope of the data would provide an estimate of the buckling load. That is, given $\delta = \delta_0/(1 - F/F_{cr})$ where δ is representative of the measured lateral deflection, δ_0 is an initial

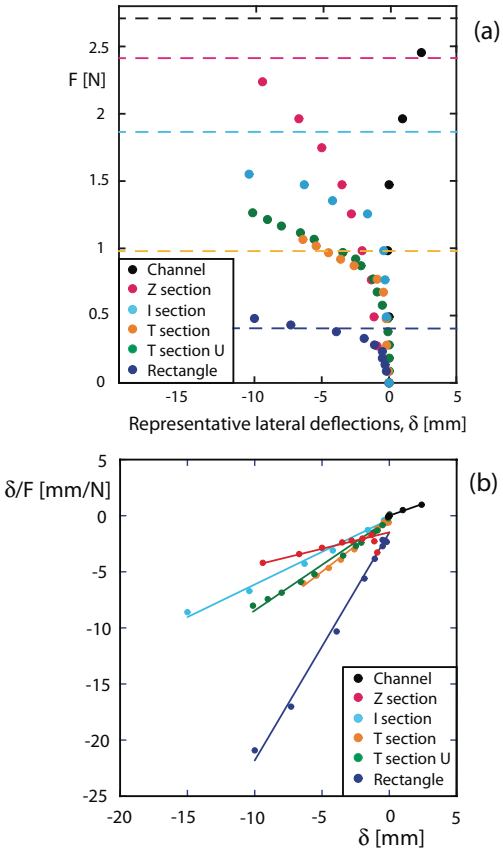

Figure 10: (a) Experimental results for the central peg for all cross-sections, and (b) alternative plot of the experimental data.

deflection, F is the measured load, and F_{cr} is the buckling load, we can re-write this expression as $\delta/F = \delta/F_{cr} + \delta_0/F_{cr}$. This is the equation of a straight line with slope $1/F_{cr}$ if δ/F is plotted as a function of δ. Figure 10(b) shows the same data from Figure 10(a) but now plotted in terms of the new axes. Each data set was fit using a linear least squares giving the estimates in Table 3. All of these estimates were based on including all the measured data, and provide reasonable estimates in comparison with the theoretical values based on the buckling analysis reported in Tables 2 and 3. These values also confirm the relative ratios suggested in Table 2. The estimate for the Z-shape, which showed the greatest disparity between theory and experiments (41% error), was based on data that showed the least amount of noticeable increasing deflection; this difference is explored in the following section. These estimates can be improved upon using various mechanisms, mostly concerning the range of applicability of the method [21, 22], but overall seem to be adequate in

terms of a comparative study seeking to shed light on the relation between cross-sectional shapes and LTB.

7.1. Numerical Validation

To validate the experimental observations from the Southwell plot, a similar analysis was performed with Fusion 360's Simulation capabilities. Whereas geometric anomalies were the source of imperfections in the experiments, a small lateral (notional) load was applied in the simulation for convenience. Figure 11 shows the load-deflection and Southwell plots for the different shapes assuming a 1% notional load. In Figure 11(a), the dashed lines indicate the LTB estimates based on a buckling analysis (see Section 4 and Table 1). As expected, the force-deflection curves asymptote to the buckling load, with the exception of the Z-shape. Because of the rotated orientation of the Z-shape's principal axes, the vertical load immediately generates a large lateral deflection. This lateral deflection dominates the buckling effect. As a result, the critical load estimates based on the Southwell plot (see Figure 11(b) and Table 3) are artificially high, as was the case for the experimental tests. The Southwell plot estimates in Table 3 for the numerical results are based on a best fit line for the highest 3 loads—20 load increments were used in all cases—because this is the portion of the results in which buckling dominates and the δ/F–δ curves asymptote to the

Table 3: LTB critical load F_{cr} [N] estimates based on buckling analysis (Table 1) and Southwell plots (Figs. 10 and 11).

		Southwell	
Cross section	Buckling	Experimental	Numerical
Rectangle	0.441	0.49	0.47
T-shape	0.957	1.08	1.07
Upside down T-shape	1.15	1.26	1.27
I-shape	1.87	1.72	1.98
Z-shape	2.41	3.40	5.61
C-channel	2.64	2.35	2.76

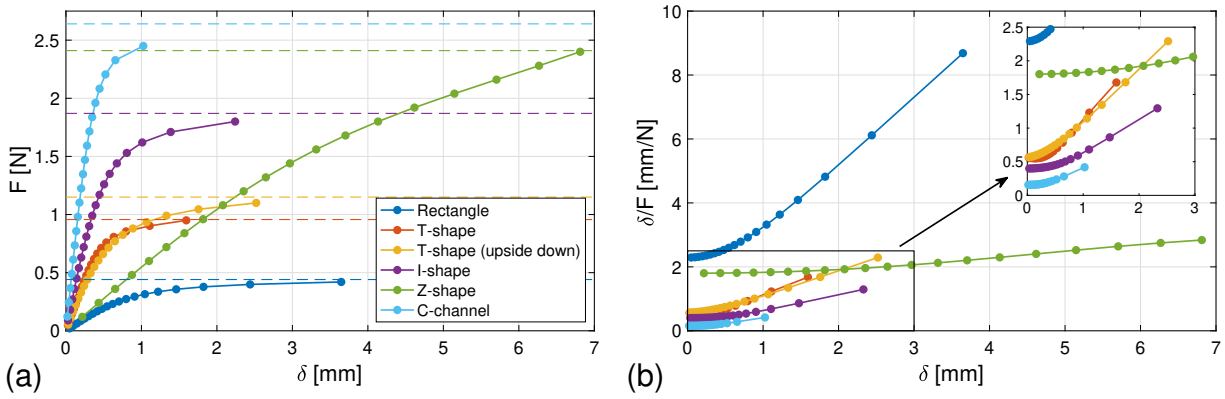

Figure 11: Numerical results from Fusion 360 for the different sections with 1% notional load: (a) Vertical force F versus lateral displacement δ midway along beam, and (b) corresponding Southwell plot.

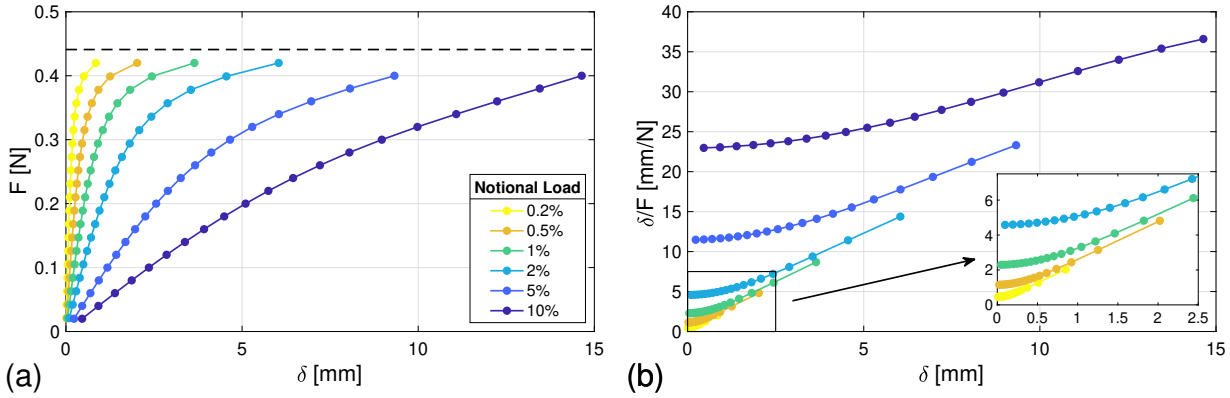

Figure 12: Southwell plot results from Fusion 360 for the rectangular section with different notional loads: (a) Vertical force F versus lateral displacement δ midway along beam, and (b) Southwell plot.

$1/F_{cr}$ slope.

To further explore the effects of this symmetry breaking, varying notional load levels were considered for the baseline rectangular section. These results are shown in Figure 12. As the notional load is increased, its effect tends to dominate the buckling behavior, turning the problem into a large-deflection problem as opposed to a buckling problem. This is reflected in the critical load estimates from the Southwell plot: F_{cr} = 0.47 N (0.2%), 0.47 N (0.5%), 0.48 N (1%), 0.50 N (2%), 0.59 N (5%), and 0.86 N (10%). Clearly, when the symmetry-breaking is larger (i.e., higher notional load), the Southwell plot estimate is worse and tends to be higher. This is similar to what is seen for the Z-shape.

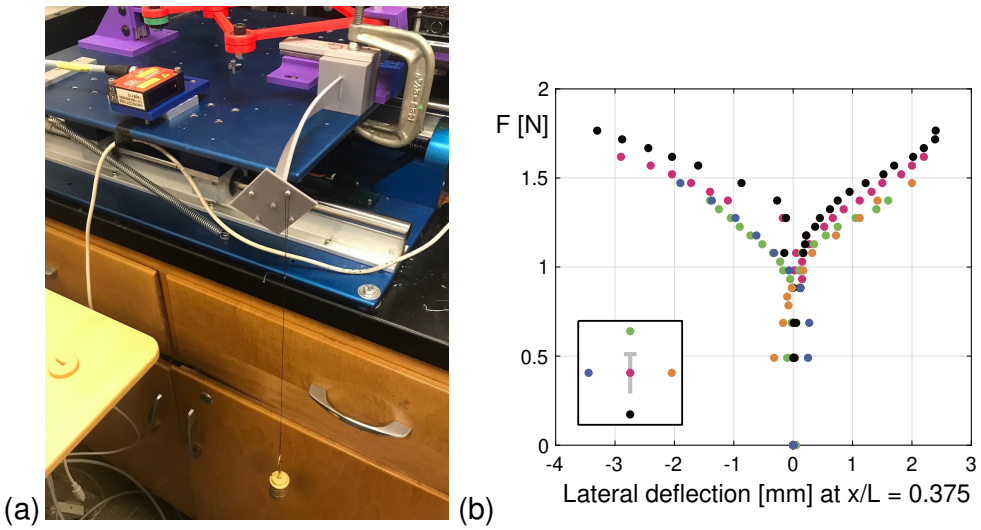

Figure 13: (a) Experimental arrangement in a different lab, and (b) experimental results for the T-shape cross-section printed with PLA.

8. Adoption by Others

As the motivation for this paper is in part educational, it is important that other educators and researchers can easily adopt and implement the demonstration model. To illustrate this, a few of the tests were repeated at the University of Oklahoma on a consumer-grade 3D printer (Prusa i3 MK3S+) using a different material (PLA). Figure 13(a) shows the experimental setup for the T-shape cross-section, and the experimental results are shown in Figure 13(b). The demonstration model was straightforward to print, albeit requiring substantial (nonsoluble) support material. Moreover, the LTB phenomenon was captured. Note the buckling load is higher for this specimen than the one shown in Figure 6. The difference is attributed to PLA having a higher Young's modulus (~3.1 GPa [23]) than ABS.

We also note that it would possible to incorporate the various cross-sections into a modular system with a common base-support, thus facilitating a direct tactile comparison as done for example for torsion in Ref. [24].

9. Discussion

This paper has focused on relatively slender cross-sectional cantilever beams, which could then be assessed according to their resistance to lateral-torsional buckling. 3D-printing allows for relatively high geometric precision.

The use of ABS thermoplastic material is not perfect however. For the C-channel and Z-shape, the higher loads seemed to have the effect of producing relatively high stress, and in some cases a kind of creep behavior (very slow but steadily increasing deflection under a constant weight) was observed. It was also apparent that this led to the unloading path not quite following the loading path, although returning to the undeflected shape *after a while*.

In all cases it should be emphasized that even when the lateral deflection at the measured point (roughly a third of the way along the beam from the clamp) was close to zero, the twist could be quite appreciable and not really reflected in the single measurement.

The areas (and hence material used) of the cross-sections are slightly different: the size of the web was kept constant between all the different sections, and thus, a strict comparison of the different sections was compromised. However, the overall trends illustrate the phenomenon of lateral-torsional buckling and its dependence on cross-sectional geometry.

Acknowledgments

This material is based upon work supported by the National Science Foundation under Grant Nos. CMMI-1926672 (LNV) and CMMI-1943917 (PSH). The opinions, findings, and conclusions, or recommendations expressed are those of the author(s) and do not necessarily reflect the views of the National Science Foundation. This support is greatly appreciated.

References

[1] S. P. Timoshenko, J. Gere, Theory of Elastic Stability, Dover, 1961.

[2] N. S. Trahair, Flexural-Torsional Buckling of Structures, CRC Press, 1993.

[3] B. W. Schafer, Local, distortional, and Euler buckling of thin-walled columns, Journal of Structural Engineering 128 (2002) 289–299. doi:10.1061/~ASCE!0733-9445~2002!128:3~289!

[4] W. Young, R. Bufynas, Roark's Formulas for Stress and Strain, McGraw-Hill, 2011.

[5] W. Zhang, L. Gardner, M. A. Wadee, M. Zhang, Analytical solutions for the inelastic lateral-torsional buckling of I-beams under pure bending via plate-beam theory, International Journal of Steel Structures 18 (2018) 1440–1463. doi:10.1007/s13296-018-0163-2.

[6] M. Z. Dietrich, A. F. G. Calenzani, R. H. Fakury, Analysis of rotational stiffness of steel-concrete composite beams for lateral-torsional buckling, Engineering Structures 198 (2019) 109554. doi:10.1016/j.engstruct.2019.109554.

[7] B. Jáger, L. Dunai, Nonlinear imperfect analysis of corrugated web beams subjected to lateral-torsional buckling, Engineering Structures 245 (2021) 112888. doi:10.1016/j.engstruct.2021.112888.

[8] R. H. Plaut, M. R. Eatherton, Lateral-torsional buckling of butterfly-shaped beams with rectangular cross section, Engineering Structures 136 (2017) 210–218. doi:10.1016/j.engstruct.2017.01.026.

[9] L. N. Virgin, Enhancing the teaching of linear structural analysis using additive manufacturing, Engineering Structures 150 (2017) 135–142. doi:10.1016/j.engstruct.2017.07.054.

[10] L. N. Virgin, Enhancing the teaching of structural dynamics using additive manufacturing, Engineering Structures 152 (2017) 750–757. doi:10.1016/j.engstruct.2017.09.052.

[11] L. N. Virgin, Enhancing the teaching of elastic buckling using additive manufacturing, Engineering Structures 174 (2018) 338–345. doi:10.1016/j.engstruct.2018.07.059.

[12] S. J. Calhoun, P. S. Harvey, Jr., Enhancing the teaching of seismic isolation using additive manufacturing, Engineering Structures 167 (2018) 494–503. doi:10.1016/j.engstruct.2018.03.084.

[13] J. M. Anderson, N. S. Trahair, Stability of monosymmetric beams and cantilevers, Journal of the Structural Division (ASCE) 98 (1972) 269–286. doi:10.1061/JSDEAG.0003114.

[14] D. A. Nethercot, The effective lengths of cantilevers as governed by lateral buckling, The Structural Engineer 51 (1973) 161–168.

[15] T. M. Roberts, C. A. Burt, Instability of monosymmetric i-beams and cantilevers, International Journal of Mechanical Sciences 27 (1985) 313–324. doi:10.1016/0020-7403(85)90021-9.

[16] C. M. Wang, S. Kitipornchai, On stability of monosymmetric cantilevers, Engineering Structures 3 (1986) 169–180. doi:10.1016/0141-0296(86)90050-7.

[17] L. N. Virgin, On the flexural stiffness of 3D printer thermoplastic, International Journal of Mechanical Engineering Education 45 (2017) 59–75. doi:10.1177/0306419016674140.

[18] R. S. Barsoum, R. H. Gallagher, Finite element analysis of torsional and lateral stability problems, International Journal of Numerical Methods in Engineering 2 (1970) 335–352. doi:doi.org/10.1002/nme.1620020304.

[19] D. A. Nethercot, K. C. Rockey, Finite element solutions for the buckling of columns and beams, International Journal of Mechanical Sciences 13 (1971) 945–949. doi:10.1016/0020-7403(71)90080-4.

[20] R. V. Southwell, On the analysis of experimental observations in problems of elastic stability, Proceedings of the Royal Society of London A 135 (1932) 601–616. doi:10.1098/rspa.1932.0055.

[21] H. H. Spencer, A. C. Walker, Critique of Southwell plots with proposals for alternative methods, Experimental Methods 15 (1975) 303–310. doi:10.1007/BF02318661.

[22] P. Mandal, C. R. Calladine, Lateral-torsional buckling of beams and the Southwell plot, International Journal of Mechanical Sciences 44 (2002) 2557–2571. doi:10.1016/S0020-7403(02)00192-3.

[23] J. H. Porter, T. M. Cain, S. L. Fox, P. S. Harvey, Jr., Influence of infill properties on flexural rigidity of 3D-printed structural members, Virtual and Physical Prototyping 14 (2019) 148–159. doi:10.1080/17452759.2018.1537064.

[24] L. N. Virgin, A shear center demonstration model using 3D-printing, International Journal of Mechanical Engineering Education Online First (2021) 1–10. doi:10.1177/03064190211057429.

Appendix A. System Identification

In comparing experimental data with theory, it is necessary to input values for the various parameters. For the small geometric parameters the actual 3D-printed dimensions tended to be slightly different from the design (nominal) values. For example, the 1-mm web thicknesses were typically measured (using calipers) around 1.05 mm, and since this parameter enters into the stiffness via the second moment of area it will produce a propagated error.

Similarly for the material properties. Previous testing of the ABS thermoplastic suggested a Young's modulus of $E = 2.1$ GPa, based on the type of flexural testing appropriate to the situation under study but also indicated the approximate nature of this estimate [17]. However, as a further confirmation of modeling, using the measured dimensions and estimated elastic properties in a FEA within Fusion 360 resulted in a fundamental natural frequency in bending of 6.38 Hz, comparing favorably with a measured frequency of 6.3 Hz.